Calculations and Measurements of the Dynamic Stark Effect in Hydrogen

W. R. Rutgers and H. W. Kalfsbeek

Association Euratom-FOM
FOM-Instituut voor Plasmafysica, Rijnhuizen, Jutphaas, The Netherlands

(Z. Naturforsch. **30 a**, 739–749 [1975]; received February 8, 1975)

A theory is given for the spectral profile of the first hydrogen Balmer line when the radiating neutral atom is under influence of both (quasi-) static and harmonically oscillating electric fields. Profiles, measured in a turbulent heating experiment, show a series of intensity maxima on the wings of the Balmer lines. If we assume a model for the spatial distribution of turbulent wave vectors, we can derive the fieldstrength and the direction of low-frequency (ion-acoustic) oscillations and the strength and frequency of high-frequency (Langmuir) oscillations.

I. Introduction

In plasmas with a strong current various electrostatic fluctuations and/or coherent waves are excited. The radiation profiles of hydrogen neutral lines can yield valuable information on the strength, frequency and direction of the accompanying electric fields. If the drift velocity of the electrons exceeds the ion-acoustic speed, $c_s = \{k(T_e + T_i)/m_i\}^{\frac{1}{2}}$, oscillations with frequency near the ion plasma frequency f_{pi} and near the electron plasma frequency f_{pe} are found to be simultaneously present, both in the experiments [1] as well as in computer simulations by Chodura [2].

In order to calculate the effect of high and low frequency micro-fields from the plasma waves on the spectral line shape of hydrogen lines, a model for the intensity of the fluctuations at each frequency f, and wave vector k, must be adopted. Sholin [3] calculated the Stark broadening in a turbulent plasma if the low frequency field distribution is described by a Rayleigh function. He found that lines without a central Stark component (Ly_β, H_β, etc.) split up due to quasi-static ion-acoustic oscillations, while the splitting is a direct measure for the average intensity of the low frequency fields. The shape of the lines with a strong central component (Ly_α, H_α, H_γ, etc.) is determined by the level of electron Langmuir oscillations, which broaden that line. Other calculations of the hydrogen line shape under influence of oscillating fields have been performed by Yakovlev [4]. In his paper the average value of the electric fieldstrength $\sqrt{\langle E^2 \rangle}$ is deduced from the moments of the electric field distribution, with the assumption that both regimes of oscillations may be treated separately. Cohn et al. [5], showed for Ly_α that resonant effects between high and low frequency fields can influence the intensity profile dramatically. This effect was found experimentally by Gallagher and Levine [6] and by Rutgers and De Kluiver [7] for the Balmer lines.

In Section II, the theory is given for the calculation of a hydrogen line if the radiating neutral is exposed to a (quasi-) static and an oscillating field. In Section III, we present numerical results of line shapes for different statistical distributions of wave vectors $\boldsymbol{k}$, of the quasi-static field. In Section IV, we describe the turbulent heating experiment, the optical measurements and the identification of the intensity maxima in the wings of the hydrogen spectral lines. In addition, the plasma state during different stages of the turbulent heating process, is briefly outlined.

The profiles are further analyzed in Section V. The validity and applicability of our model for the derivation of turbulent micro-fields from the dynamic Stark effect are discussed.

Reprint requests to W. R. Rutgers, FOM-Instituut voor Plasmafysica, *Rijnhuizen*, Jutphaas, The Netherlands.

II. Theory

We assume each radiating atom to be exposed to an electric field as proposed in Ref. 7, being the sum of a quasi-static and a harmonically oscillating field:

$$\boldsymbol{E} = \boldsymbol{E}^S \cos(\Omega_S t) + \boldsymbol{E}^D \cos(\Omega_D t + \Phi), \Omega_S \ll \Omega_D . \quad (1)$$

Henceforth, the time dependence of the low frequency field is neglected: $\Omega_S = 0$ (see Section V for justification). The field is thought to be homogene-

ous during the radiation process and axial symmetry is accepted. The z-axis is chosen as the axis of symmetry and we write $\boldsymbol{E} = \boldsymbol{E}_{\parallel} + \boldsymbol{E}_{\perp}$

$$\boldsymbol{E}_{\parallel}(t) = E_{\parallel}^{\mathrm{S}}\,\hat{z} + E_{\parallel}^{\mathrm{D}} \cos(\Omega_{\mathrm{D}} t + \Phi_{\parallel})\,\hat{z}, \qquad (2)$$
$$\boldsymbol{E}_{\perp}(t) = E_{\perp}^{\mathrm{S}}(\hat{x}+\hat{y}) + E_{\perp}^{\mathrm{D}} \cos(\Omega_{\mathrm{D}} t + \Phi_{\perp})\,(\hat{x}+\hat{y});$$

$\hat{r}_{\sigma} = \hat{x}, \hat{y}, \hat{z}$ is a unity vector in direction σ. This field gives rise to an extra term H_1 in the Hamiltonian of the hydrogen atom: $H_1 = -e\,\boldsymbol{r}\cdot\boldsymbol{E}(t)$. If Eq. (2) is substituted for the electric field

$$H_1(t) = -e\,E_{\parallel}^{\mathrm{S}}\,z - e\,E_{\perp}^{\mathrm{S}}\,(x+y)$$

for $t<0$ and

$$H_1(t) = -e\{E_{\parallel}^{\mathrm{S}} + E_{\parallel}^{\mathrm{D}} \cos(\Omega_{\mathrm{D}} t + \Phi_{\parallel})\}\,z - e\{E_{\perp}^{\mathrm{S}} + E_{\perp}^{\mathrm{D}} \cos(\Omega_{\mathrm{D}} + \Phi_{\perp})\}\,(x+y) \qquad (3)$$

for $t \geqq 0$. The reason for putting $\boldsymbol{E}^{\mathrm{D}} = 0$ for $t<0$ will be discussed later. The total Hamiltonian for the atomic system is now given by:

$$H = H_0 + H_{\mathrm{r}} + H_1 \quad \text{with} \quad H_0 = \frac{p^2}{2m} + V(r),$$

for the unperturbed atom; $H_{\mathrm{r}} = -(e/m)\boldsymbol{A}\cdot\boldsymbol{p}$ describes the interaction with the radiation field; H_1 is given by Equation (3).

For the solution of the time dependent Schrödinger equation, however, we may neglect H_{r} because the influence of the radiation field E_{r} ($E_{\mathrm{r}} < 100$ V/m) is negligible with respect to turbulent micro-fields ($\tilde{E} \approx 10^7$ V/m). For the studied plasmas we also neglect the Holtzmark field ($E_{\mathrm{H}} \approx 10^4$ V/m) which arises from electrostatic ion fluctuations. The turbulent micro-fields are in turn much smaller than the interior atomic fields ($E \approx 10^{11}$ V/m) so H_1 does not induce transitions between main quantum states n and n'. Each main quantum state n however, splits up into n^2 sub-states. We consider transitions between these sub-states with slightly different energy and calculate the population density as a function of time for $t>0$, starting from a correct population at $t=0$. The time dependent Schrödinger wave function for state n, satisfies the equation:

$$i\hbar\,\frac{\partial \psi_n(t)}{\partial t} = [H_0 + H_1(t)]\,\psi_n(t)\,. \qquad (4)$$

We write

$$\psi_n(t) = \sum_l \sum_m C_{lm}^{(n)}(t)\,|n,l,m\rangle \equiv \sum_{j=1}^{n^2} C_j^{(n)}(t)\,|n,j\rangle\,, \qquad (5)$$

thus choosing the eigenfunctions $|n,l,m\rangle$ of H_0 as a base for the n^2 dimensional sub-space of the Hilbert space for the hydrogen atom. n, l and m, are the usual quantum numbers for energy (n), linear momentum (l) and angular momentum (m). Substitution of Eq. (5) into Eq. (4) yields for the coefficients $C_j^{(n)}(t)$:

$$\frac{\partial C_j^{(n)}(t)}{\partial t} = \frac{1}{i\hbar}\,[\varepsilon^{(n)}\,C_j^{(n)}(t) + \sum_{k=1}^{n^2} \langle n,j|\,H_1^{(n)}(t)\,|n,k\rangle\; C_k^{(n)}(t)] \qquad (6)$$

where $\varepsilon^{(n)}$ denotes the energy associated with the eigenfunction $|n,j\rangle$ with $H_0\,|n,j\rangle = \varepsilon^{(n)}\,|n,j\rangle$. Introducing $a_j^{(n)}(t)$ by

$$C_j^{(n)}(t) \equiv \exp\left\{-\frac{1}{i\hbar}\,\varepsilon^{(n)}\,t\right\} a_j^{(n)}(t)\,. \qquad (7)$$

Equation (6) can be written as

$$\frac{\partial a_j^{(n)}(t)}{\partial t} = \frac{1}{i\hbar} \sum_{k=1}^{n^2} \langle n,j|\,H_1^{(n)}(t)\,|n,k\rangle\; a_k^{(n)}(t)\,. \qquad (8)$$

This is a set of n^2 coupled linear differential equations with time dependent coefficients for the $a_j^{(n)}(t)$. The formal solution of this set yields

$$a_j^{(n)}(t) = \sum_{k=1}^{n^2} [\delta_{jk} + \sum_{l=1}^{\infty} \int_0^t \mathrm{d}t_1 \int_0^{t_1} \mathrm{d}t_2 \ldots \int_0^{t_{l-1}} \mathrm{d}t_l \sum_{\sigma_1=1}^{n^2} \sum_{\sigma_2=1}^{n^2} \ldots \sum_{\sigma_{l-1}=1}^{n^2} A_{j\sigma_1}^{(n)}(t_1)\,A_{\sigma_1\sigma_2}^{(n)}(t_2) \ldots A_{\sigma_{l-1}\sigma k}^{(n)}(t_l)]\,a_k^{(n)}(0)\,,$$

where $A_{jk}^{(n)}(t) = 1/i\hbar\,\langle n,j|\,H_1^{(n)}(t)\,|n,k\rangle$, because the time dependence of the matrices $A_{jk}^{(n)}(t)$ is continuous and there are no infinities in each of the integration paths.

The desired probability of occupation of a substate j, at time t, $C_j^{(n)*}(t)\,C_j^{(n)}(t)$, follows from the substitution of solutions of Eq. (8) in Equation (7). To solve the set of Eqs. (8) one must choose a proper population of the substates at $t \leqq 0$. In our model we take the eigenstates of the Hamiltonian $H_0 + H_1$ to be uniformly populated at $t=0$. The corresponding values of the coefficients $a_k^{(n)}(t)$ are such as to give the Schrödinger spectrum for the static Stark effect [8]. Physically this means that the atom is exposed to a static electric field

$$\boldsymbol{E} = E_{\parallel}^{\mathrm{S}}\cdot\hat{z} + E_{\perp}^{\mathrm{S}}\,(\hat{x}+\hat{y})$$

which starts at a value 0 at $t=-\infty$ and approaches adiabatically its value $\sqrt{(E_{\parallel}^{\mathrm{S}})^2}$ at $t=0$. $E_{\perp}^{\mathrm{S}})^2 + 2(E$

At the same time, the dynamic field is switched on. The radiated power for an atomic dipole transition from state $|n\rangle$ to state $|n'\rangle$ is according to Bethe and Salpeter [9],

$$I^{\sigma}_{nn'} = \frac{\omega^4_{nn'}}{3\,c^3\,\pi\,\varepsilon_0}\,[\mu^{\sigma}_{n'n}]^*\,\mu^{\sigma}_{n'n} \quad \text{where} \qquad (9)$$

$\omega_{n'n} \equiv \frac{1}{\hbar}\,(\varepsilon^{(n)} - \varepsilon^{(n')})$ is the Bohr frequency,

$$\mu^{\sigma}_{n'n} = \langle \psi_{n'} | \boldsymbol{e}_{\sigma}\cdot\boldsymbol{r} | \psi_n \rangle = \mu^{\sigma *}_{nn'} \qquad (10)$$

is the dipole matrix element of the emitted light with polarization direction $\sigma(\boldsymbol{e}_{\sigma} = \hat{x}, \hat{y}, \hat{z})$. Substitution of Eq. (5) into Eq. (10) yields

$$\mu^{\sigma}_{n'n}(t) = \sum_{k=1}^{n'^2}\sum_{j=1}^{n^2}[a_k^{(n')}(t)]^*\,a_j^{(n)}(t)\ldots$$
$$\ldots\langle n', k | r^{\sigma} | n, j\rangle \exp\{-i\,\omega_{n'n}\,t\}, \quad \text{where} \qquad (11)$$

$r^{\sigma} = x, y, z.$

The observable quantity, the spectral intensity profile for transitions between a group of upper levels (n, k) to a group of lower levels (n', j) is the Fourier transform of Eq. (9):

$$J^{\sigma}(\omega) = \frac{\omega^4}{3\,c^3\,\pi\,\varepsilon_0\,(2\,\pi)^2}\lim_{T\to\infty}\frac{1}{T} \qquad (12)$$
$$\text{Trace}\left\{\int_0^T dt\, e^{i\omega t}\,[\mu^{\sigma}_{n'n}(t)]^*\,\rho_0\int_0^T dt'\, e^{-i\omega t'}\,\mu^{\sigma}_{n'n}(t')\right\}.$$

ρ_0 is the statistical density matrix for the initial state ψ_n; it gives the population density at time $t = 0$ of the substates $|n, j\rangle$, $j = 1, 2, \ldots, n^2$. With the previous assumptions the final expression for the intensity profile is

$$J^{\sigma}(\omega) = \frac{\omega^4}{3\,\pi\,\varepsilon_0\,c^3\,(2\,\pi)^2}\lim_{T\to\infty}\frac{1}{T}$$
$$\left|\int_0^T dt\,\exp\{i(\omega-\omega_{n'n})t\}\sum_{k=1}^{n'^2}\sum_{j=1}^{n^2}\right. \qquad (13)$$
$$\left.[a_k^{(n')}(t)]^*\,a_j^{(n)}(t)\,\langle n', k | r^{\sigma} | n, j\rangle^2\right.$$

This expression has been used to calculate the transition $n = 3$ to $n' = 2$. The coefficients $a_k^{(n)}(t)$ are numerically solved from Equation (8). The perturbation matrices $H_1^{(2)}$ and $H_1^{(3)}$ are given in Table 1 and Table 2, the dipole matrices, $\langle n', k | r^{\sigma} | n, j\rangle$, are taken from Reference [9].

Table 1. Hamiltonian Matrix $H_1^{(2)}$.

$n\,l\,m$	211	210	21-1	200
211	0	0	0	$\frac{3}{2}A\sqrt{2}(1-i)$
210	0	0	0	$3B$
21-1	0	0	0	$\frac{3}{2}A\sqrt{2}(1+i)$
200	$\frac{3}{2}A\sqrt{2}(1+i)$	$3B$	$\frac{3}{2}A\sqrt{2}(1-i)$	0

Table 2. Hamiltonian matrix $H_1^{(3)}$.

$n\,l\,m$	322	321	320	32-1	32-2	311	310	31-1	300
322	0	0	0	0	0	$\frac{9}{2}A(1-i)$	0	0	0
321	0	0	0	0	0	$\frac{9}{2}B$	$\frac{9}{2}A\sqrt{2}(1-i)$	0	0
320	0	0	0	0	0	$-\frac{3}{4}A\sqrt{6}(1+i)$	$3\sqrt{3}B$	$-\frac{3}{4}A\sqrt{6}(1-i)$	0
32-1	0	0	0	0	0	0	$\frac{9}{4}A\sqrt{2}(1+i)$	$\frac{9}{2}B$	0
32-2	0	0	0	0	0	0	0	$\frac{9}{2}A(1+i)$	0
311	$\frac{9}{2}A(1+i)$	$\frac{9}{2}B$	$-\frac{3}{4}A\sqrt{6}(1-i)$	0	0	0	0	0	$3\sqrt{3}A(1-i)$
310	0	$\frac{9}{4}A\sqrt{2}(1+i)$	$3\sqrt{3}B$	$\frac{9}{4}A\sqrt{2}(1-i)$	0	0	0	0	$3\sqrt{6}B$
31-1	0	0	$-\frac{3}{4}A\sqrt{6}(1+i)$	$\frac{9}{2}B$	$\frac{9}{2}A(1-i)$	0	0	0	$3\sqrt{3}A(1+i)$
300	0	0	0	0	0	$3\sqrt{3}A(1+i)$	$3\sqrt{6}B$	$3\sqrt{3}A(1-i)$	0

$[A \equiv -e\,a_0 E^{s}_{\perp} - e\,a_0\,E^{D}_{\perp}\cos(\Omega_D\,t + \Phi_{\perp})$ and $B \equiv -e\,a_0\,E^{s}_{\parallel} - e\,a_0\,E^{D}_{\parallel}\cos(\Omega_D + \Phi_{\parallel})]$.

III. Numerical Results

In this section we will present some of the results of the calculational procedure developed in the previous section. Spectra will be exhibited for various combinations of the static and dynamic fields $\boldsymbol{E}^{\mathrm{S}}$ and $\boldsymbol{E}^{\mathrm{D}} \cos \Omega_{\mathrm{D}} t$. In Fig. 1 the geometrical relation between fields and direction of observation is shown schematically. The I_{π}-spectrum is observed through a polarizer which only transmits light with a polarization vector parallel to the axis of symmetry (z-axis). I_{σ} denotes the spectrum when the polarizer is turned 90°. The direction of observation is always perpendicular to the axis of symmetry, as in the actual experiment. The I_{π}-spectrum is calculated from Eq. (13) taking $r^{\sigma} \equiv z$, whereas the I_{σ}-spectrum is an observational average of $J^{x}(\omega)$ and $J^{y}(\omega)$ when rotating the x-y-frame around the z-axis.

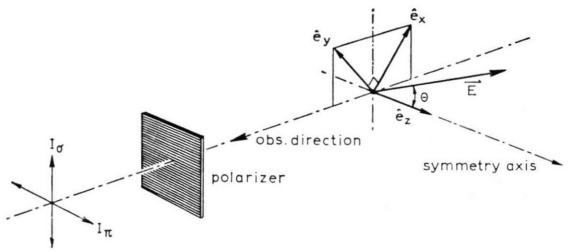

Fig. 1. Coordinate frame for the calculation of parallel (π) and perpendicular (σ) intensity profiles. θ is the angle between electric field vector $\boldsymbol{E}$ and the axis of symmetry.

In the following we will use dimensionless field-strengths:

$$E^{\mathrm{S}}_{\|,\perp} \equiv E_{\omega} \cdot S_{\|,\perp} \quad \text{and} \quad E^{\mathrm{D}}_{\|,\perp} \equiv E_{\omega} \cdot D_{\|,\perp}$$

where E_{ω} follows from $\frac{3}{2} a_0 e E_{\omega} = \hbar \Omega_{\mathrm{D}}$, Ω_{D} is the angular frequency of the dynamic field.

In Fig. 2 a series of basic spectra are shown. When there is only a parallel static field ($S_{\perp} = D_{\perp} = D_{\|} = 0$) the Schrödinger spectrum [8] is recovered (see Figure 2 a).

Figure 2 b shows the case when there is a perpendicular static field in the x and y direction. The σ-spectrum is the sum of parallel components of $E_z = E^{\mathrm{S}}_{\|}$ and σ-components of $E_x + E_y = \sqrt{2}\, E^{\mathrm{S}}_{\perp}$.

In Fig. 2 c, when there is only an oscillating field, a Blochinzew spectrum [10] is retrieved. A series of satellites is found at position $\pm n \Omega_{\mathrm{D}}$, $n = 0, 1, 2, \ldots$, with decreasing intensities.

In a second series (Fig. 3) we observe the influence of a dynamic field with frequency Ω_{D}, on the static-Stark spectrum. In the case of $S_{\perp} = D_{\perp} = 0$

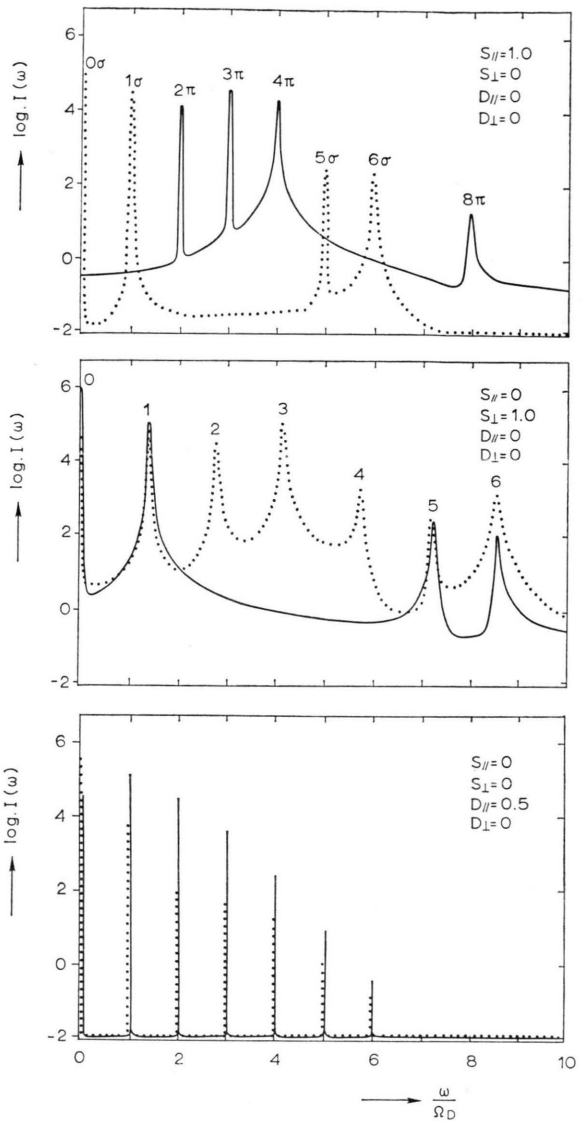

Fig. 2. I_{σ} (dotted) and I_{π} (full line) spectrum of H_{α}. $\omega = 0$ is the unperturbed position. (a) Static field along the symmetry axis; (b) Static field perpendicular to the axis of symmetry; (c) Oscillating field with angular frequency Ω_{D}.

(Fig. 3 a) to each static-Stark component a series of harmonic satellites at position $\pm n \Omega_{\mathrm{D}}$ appears with the same polarization as the Stark component. When the static and the dynamic field are at right angles (Fig. 3 b), ($S_{\perp} = D_{\|} = 0$), the Stark components and the satellites are polarized in an opposite direction. When the angle between static and harmonic field is arbitrary (Fig. 3 c), a mixture of the two previous patterns is found. Note that the positions

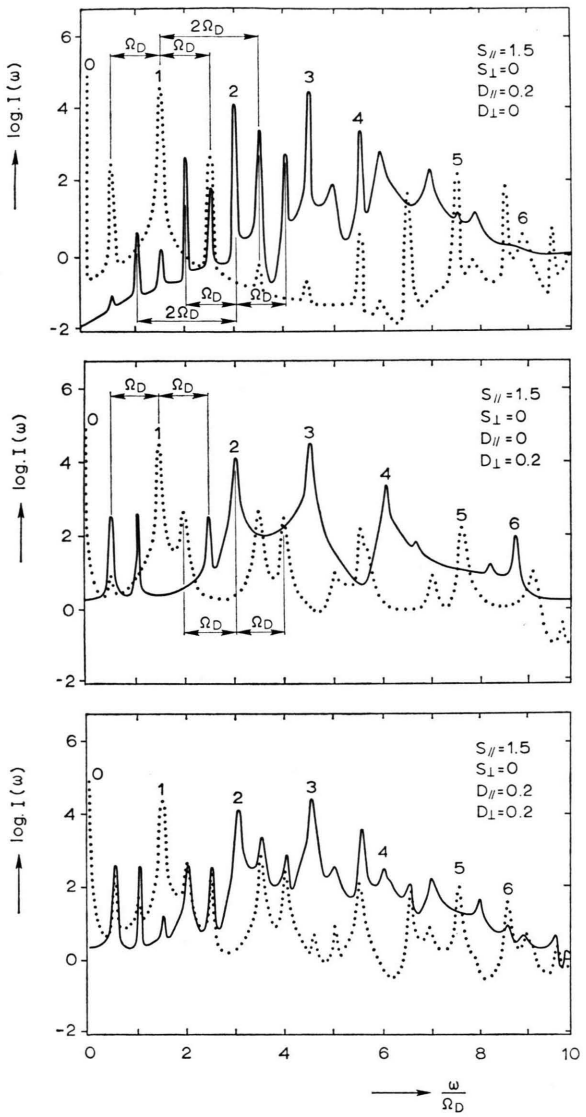

Fig. 3. Combinations of static and dynamic fields. (a) Satellites and ± n. Ω. from the Stark components 0, 1, 2, ... etc. with same polarization ($S \parallel D$); (b) Satellites with opposite polarization ($S \perp D$); (c) Combination of (a) and (b).

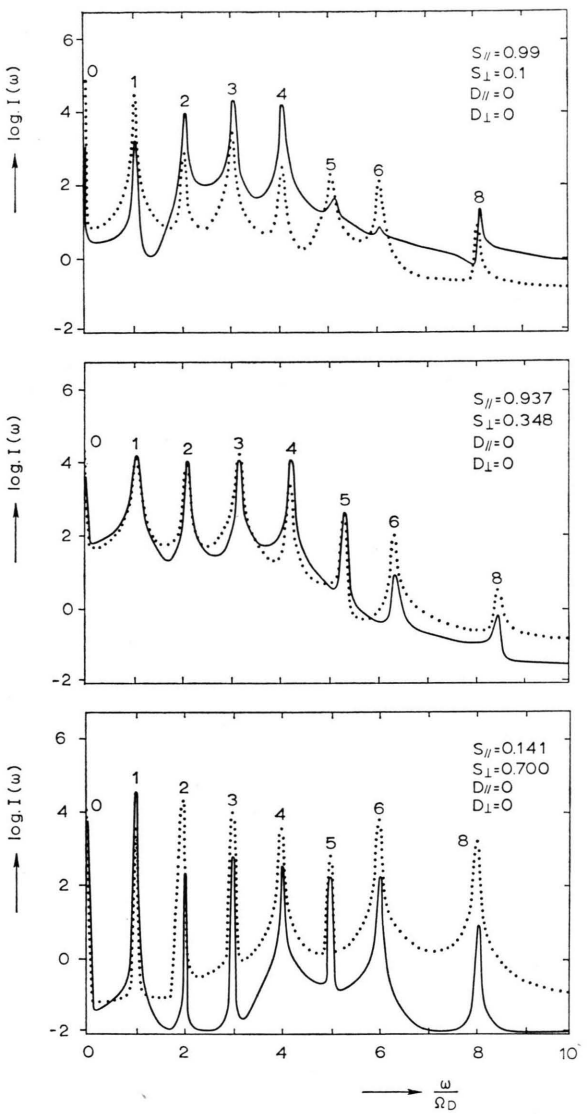

Fig. 4. Combinations of parallel and perpendicular static fields. (a) $\theta \approx 8°$, (b) $\theta \approx 28°$, (c) $\theta \approx 82°$. $\operatorname{tg}\theta = \sqrt{2}\, S_{\perp}/S_{||}$.

of the intensity maxima are not affected by this angle, only the mutual height ratios are changed.

In Fig. 4 the effect of changing the ratio $S_{\perp}/S_{||}$ is shown, keeping $S=\sqrt{S_{\parallel}^2+2\,S_{\perp}^2}$ constant. When the total static electric fieldstrength vector is at an angle θ of approximately 30° to the z-axis, the observed π and σ spectra show very little difference, (Fig. 4 b). At greater angles, the role of π and σ reverses (Fig. 4 c; $\theta \sim 80°$). In Fig. 5 effects of resonance between static and oscillating fields are shown. Resonance occurs when the frequency difference between the static components

$$\Delta = 3\, a_0\, e\, |\boldsymbol{E}^{\mathrm{S}}|/2\,h\,,$$

matches the frequency $f=\Omega_{\mathrm{D}}/2\,\pi$ of the oscillating field. The two mean effects of resonance are:

1. The Stark components are broadened (Fig. 5 b) and, at sufficiently strong fieldstrengths, splitted into an intricate fine structure pattern (Fig. 5 c).

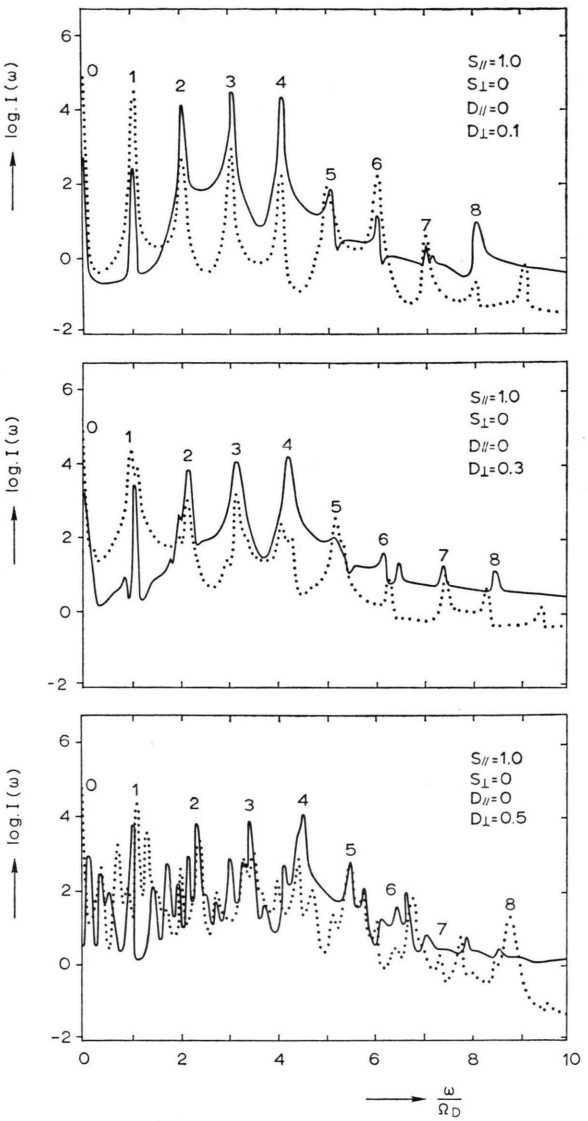

Fig. 5. Resonance between static and dynamic fields: the Stark splitting constant Δ equals the frequency Ω_D of the oscillating field. (a) $|E^S_{\parallel}|/|E^S_{\parallel}|=10\sqrt{2}$, (b) $|E^S|/|E^D|=10/3\sqrt{2}$, (c) $|E^S|/|E^D|=10/5\sqrt{2}$.

2. Forbidden components (e.g. at $f=7\,\Delta$ and $9\,\Delta$) appear.

These features occur regardless of the direction of the dynamic field with respect to the static field and cannot result from any perturbation theory.

In the next two figures we present and interpret spectra for more sophisticated spatial statistical distributions of static and time-dependent electric fields. From theories and measurements of fluctuation spectra in turbulent plasmas it is reasonable to assume the following distribution of static field vectors $\boldsymbol{E}^S$ and dynamic field vectors $\boldsymbol{E}^D$:

Static field vectors

are parallel to propagation vectors $\boldsymbol{k}_{ac}$ of ion-acoustic waves. These waves are unstable when $\boldsymbol{k}_{ac}$ lies within the Cerenkov cone (vertex angle $\theta_{cer}=\arccos c_s/u$, where u is the drift velocity, and c_s is the ion-acoustic speed). Spectra are calculated for angles θ_S of the vertex of a cone ($\operatorname{tg}\theta_S=\sqrt{2}\,S_\perp/S_{||}$) keeping cylindrical symmetry and a constant magnitude for the static fieldstrength $|\boldsymbol{E}^S|=E_\omega\sqrt{S_\parallel^2+2\,S_\perp^2}\equiv E_\omega\cdot S$.

Dynamic field vectors

$\boldsymbol{k}_L$ of the Langmuir oscillations are taken to be isotropic in space. The distribution is chosen such that the endings of the tips of the field vectors cover homogeneously the surface of a sphere with radius $|\boldsymbol{E}^D|=E_\omega\sqrt{D_\parallel^2+2\,D_\perp^2}$. The combined effect of the static and the dynamic fields is approximated by a spectrum, composed of the weighted sum of spectra for nine values of $\theta_D=\operatorname{arctg}\sqrt{2}\,D_\perp/D_{||}$, and values of θ_S between $\theta_S=0$ and $\theta_S=\theta_{cer}$. In general, the spectral shape depends on the angle of the Cerenkov cone, on the ratio between the Stark splitting constant Δ and the frequency $f=\Omega_D/2\pi$ of the oscillating field, and on the strength of the dynamic field.

In Fig. 6 and Fig. 7 the effect of perpendicular static and of oscillating fields on the static Stark spectrum is illustrated, where a linear intensity scale is used in contrast with previous spectra. A simultaneous presence of all static components in both polarizations can be observed if θ_{cer} essentially differs from zero (Fig. 6 a, $D=0$; $\theta_{cer}\approx 45°$; $\Delta/f=0.8$). Adding a small dynamic field results in satellites separated at frequencies $n\cdot\Omega_D$ (integer n) from each static component (Fig. 6 b, $D=0.4$; $\theta_{cer}\approx 45°$; $\Delta/f=1.5$). When the fieldstrength of the dynamic field is increased, the static components, denoted as 1, 2, 3, ..., etc. are broadened whereas the intensity difference amongst the components decreases (Fig. 6 c, $D=0.8$; $\theta_{cer}\approx 45°$; $\Delta/f=1.5$). An additional effect if $|\boldsymbol{E}^D|>\frac{1}{2}|\boldsymbol{E}^S|$ is the appearance of satellites at $n\cdot\Omega_D$ from the unperturbed position denoted as I, II, ... in Fig. 7 a ($D=0.5$; $\theta_{cer}\approx 25°$; $\Delta/f=0.8$). The spectrum is complicated and less useful for easy deduction of fieldstrength parameters. The origin of the intensity maxima is not simply recovered unless the satellites at $n\,\Omega_D$ and the static

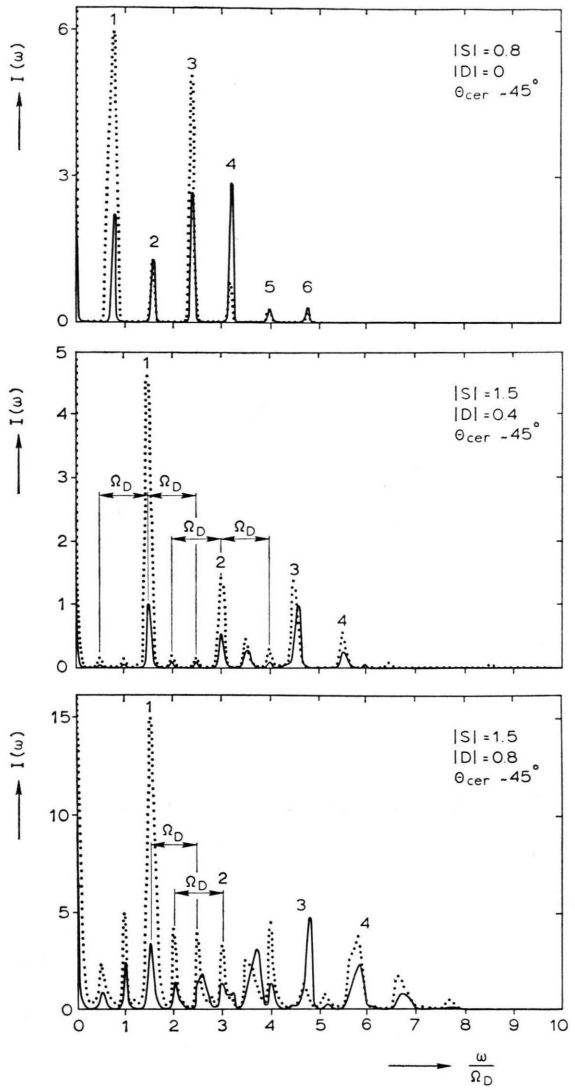

Fig. 6. Calculations for static fluctuations filling the Cerenkov cone. (a) Static fields only, (b) Small dynamic field, (c) Strong dynamic field.

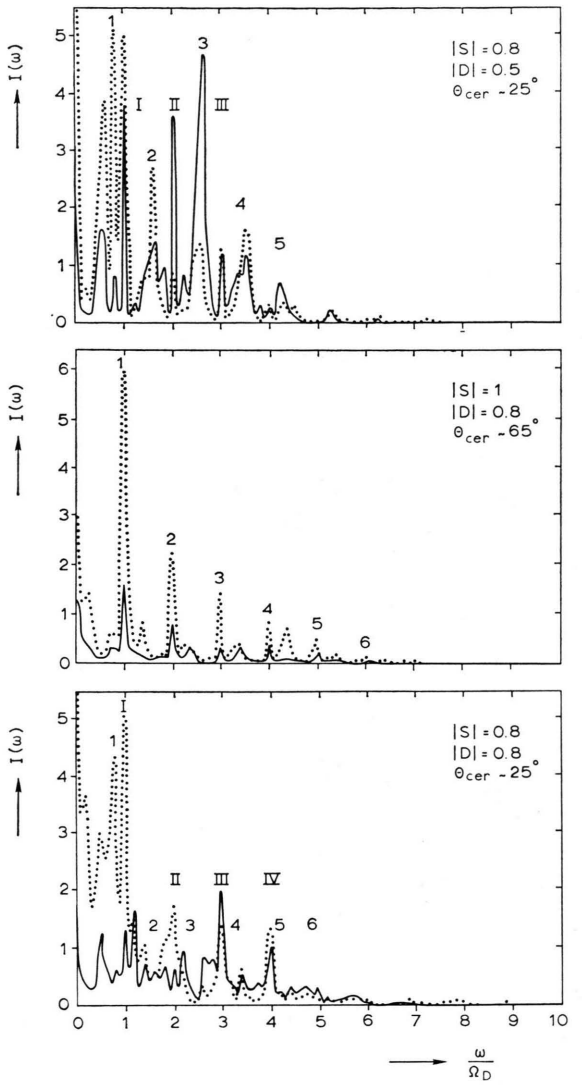

Fig. 7. (a) As Fig. 6 c but now for $\Delta/f=0.8$, (b) Strong resonant field, (c) Dominating dynamic field.

components coincide. This can be seen in Fig. 7 b ($D=0.8$; $\theta_{cer} \approx 65°$; $\Delta/f=1$), where a case of resonance is shown.

When the dynamic fieldstrength exceeds the static fieldstrength, the line shape gradually passes into a pure Blochinzew spectrum (see Figure 2). In Fig. 7 c ($D=0.8$; $\theta_{cer} \approx 25°$; $\Delta/f=0.8$) a spectrum is shown for equal static and dynamic fieldstrengths. Pronounced maxima at $n\,\Omega_D$ from the unperturbed position can be observed and obviously it is no longer possible to deduce $|\boldsymbol{E}^S|$ from the spectral profile.

IV. The Experiment

The experiments on turbulent heating have been carried out with a hollow-cathode arc discharge, length 0.8 m, diameter 0.03 m. The arc is running on the axis of a magnetic mirror field with magnetic induction up to 2 Tesla and mirror ratio 1.6. The electron plasma density can be varied between 2×10^{19} and $2\times10^{20}\,m^{-3}$ and the electron temperature in the arc is between 5 eV and 15 eV initially.

By discharging a high voltage capacitor (1.8 μF, 40 kV) across the plasma column, current-driven micro-instabilities are excited in the plasma resulting

in rapid electron and ion heating. A description of the apparatus and results (Turhe II) on ion and electron temperatures, heating efficiencies and energy densities are given by Piekaar [11]. The resistivity of the plasma during the turbulent phase, when a high level of electrostatic fluctuations is present, was measured by Schrijver [12] under widely different conditions of electric field along the column, plasma density and ion mass. Recent results, obtained in the Turhe III device equipped with a higher magnetic field, are reported by Schrijver [13]. Temperatures up to $T_e = 10$ keV and $T_i = 3$ keV have been measured.

The profiles of the Balmer lines H_α, H_β and H_γ have been measured (see Figs. 8, 9, and 10) photoelectrically with a 1 m monochromator in side-on observations. The profiles were scanned from shot to shot in wavelength steps of 1/3 Å and averaged over two to four successive discharges. The measured profiles (see also Ref. 7) show a series of satellites on the wings of lines with (H_α, H_γ) and without (H_β) a central component. The intensity of these maxima is rather insensitive to the direction of a polarizer between plasma and monochromator. Besides, mutual intensity ratios of the various maxima do not correlate with those calculated by Schrödinger for the static Stark effect. On the other hand, the position of the maxima is in accordance with a static Stark spectrum.

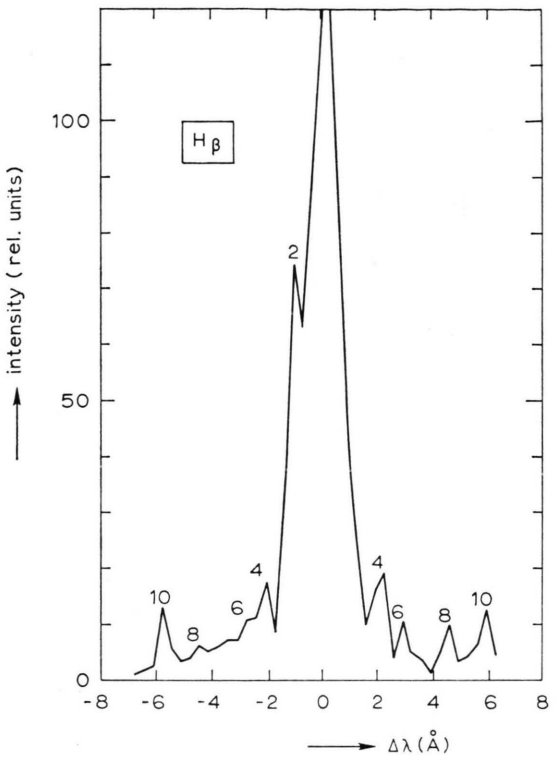

Fig. 9. H_β line profile.

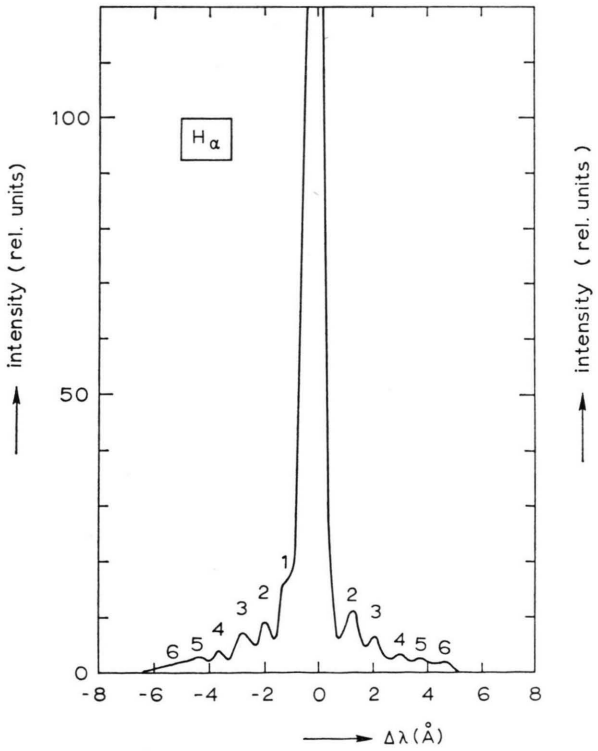

Fig. 8. H_α line profile for $n = 10^{20}$ m^{-3}, $E_0 = 19$ kV/m.

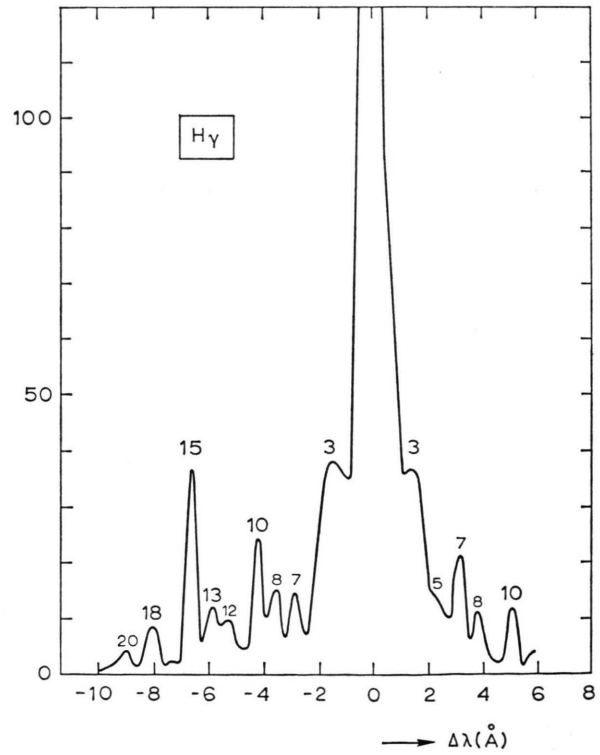

Fig. 10. H_γ line profile.

The turbulent heating experiment lasting a few microseconds can be considered as a succession of three phases. During all stages, the electrical field is far above the runaway threshold. In the first phase, $T_e/T_i \gg 1$, and the drift velocity u, exceeds the electron thermal velocity v_{the}. A strong two-stream instability develops and e.m. radiation near the characteristic frequency for this instability $f^* = 0.5 f_{pe} (m_e/m_i)^{1/3}$ is observed. Due to a rapid increase of T_e, the drift velocity drops below v_{the} and a gradual transition into a second phase starts.

During this stage u remains larger than the ion-acoustic speed $c_s = \{k(T_e + T_i)/m_i\}^{\frac{1}{2}}$, $(c_s < u < v_{the})$, and the ion-acoustic drift instability prevails. The plasma emits e.m. radiation near f_{pi} and f_{pe} due to a high level of acoustic and Langmuir oscillations in the plasma *. The hydrogen profiles have been measured during this stage, in which ions are heated up to keV temperatures.

The third stage may be characterized by a decrease in T_e/T_i to an ultimate value of $T_e/T_i \approx 3$. The macroscopic value of u/c_s drops to about 1 to 2 and the growth rate of the ion-acoustic instability is small. Under certain conditions the quenching of the instability is preceded by a current dip, strong e.m. radiation at ω_{pe} and harmonics, and bursts of X-ray radiation.

V. Applications of the Numerical Calculations

Instead of the δ-function distribution used for the electric fields it is also possible to calculate the line shape for a distribution of oscillating fields which is described by e.g. a Rayleigh function used by Sholin [3] and Babykin [14], or a Gauss-function used by Raether [15]. These distributions are not likely to occur in our experiment because they cannot account for the peaks on the wings of the measured line profiles. The radiating atoms in the turbulent heating experiment are not exposed to a static and harmonic field but rather to a combination of two harmonic fields: one with frequency near the ion plasma frequency, f_{pi}, due to fields of ion-acoustic mode and the other near the electron plasma frequency, f_{pe}, $(\approx 45 f_{pi})$ due to Langmuir waves. The Holtzmark fields and radiation fields are also present but are orders of magnitude smaller than the above-mentioned harmonic fields.

* The existence of these oscillations is also evident from measurements of He line profiles where "forbidden lines", due to low frequency fluctuations, have been measured together with satellites at $\pm f_{pe}$, caused by high frequency oscillations [13]. These measurements will be discussed in a separate publication.

We will now investigate in more detail the effect of a harmonic field $E \cos 2\pi f t$ of arbitrary frequency f in relation to the Stark splitting constant Δ caused by the amplitude E. With Yakovlev we know that in the limit $\Delta/f \gg 1$, the shape of the k'th Stark component consists of a series of spikes, separated by f. The envelope of the spikes is sharply peaked at $k\Delta$; accurately the position of the component k for a completely static field. The spectrum for $\Delta/f \lesssim 1$ consists of a series of spikes with decreasing intensity (Blochinzew spectrum).

From the value of the anomalous resistance and from the intensity of forbidden lines in the helium spectrum we know that the energy in the oscillations is of the order of 1‰ to 1% of the thermal energy in the plasma. This means that we are dealing with values of the ratio Δ_S/f_S typically between 50 and 200 for the low frequency fields so that we can use the quasistatic approach for the ion-acoustic mode. On the other hand, the ratio Δ_D/f_D for the high frequency fields is of the order of 1 or even smaller. With the statistical model for the fields and for the parameters considered, a comparison between calculated profiles and measured profiles is justified.

From the position of the identified Stark components of the H_α, H_β and H_γ line profiles (see Figs. 8, 9 and 10) the fieldstrengths of low frequency microfields $|\boldsymbol{E}^S|$ can be calculated. Results are presented in Fig. 11 for various values of E_0, the field applied to the plasma column to excite the micro-

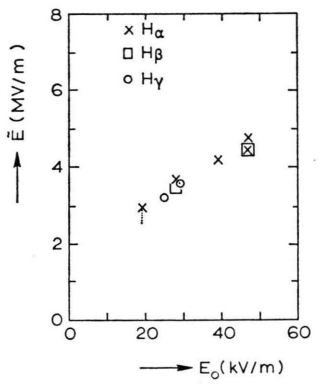

Fig. 11. Fieldstrength $\tilde{E}$ of the low frequency microfields, deduced from the separation of Stark components, versus applied electric field E_0.

instabilities. The fieldstrength E_S lies between 2 and 5×10^6 V/m. Therefore with a density of 10^{20} m^{-3} the ratio Δ_S/f_D, denoted as Δ/f, varies from $\frac{1}{2}$ to 1 ($f_{pe} \sim 90$ GHz corresponding to 1.3 Å for the H_α

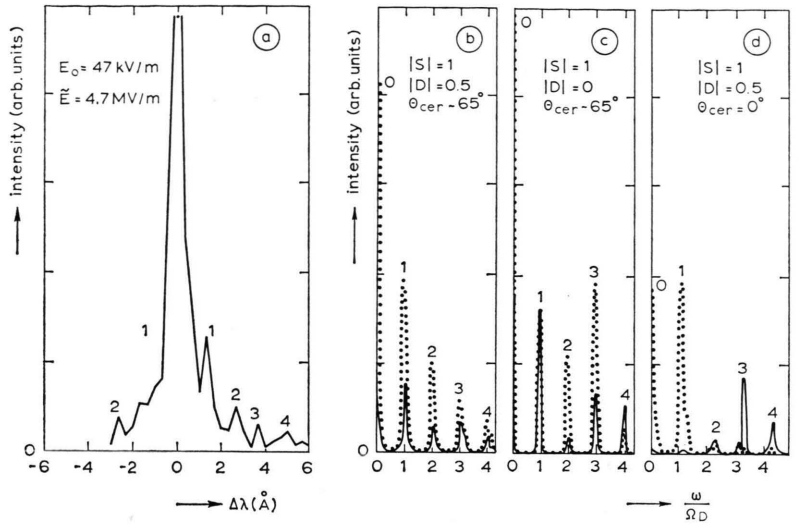

Fig. 12.
(a) Measured H_α profile for applied field $E_0 = 47$ kV/m and electron density $n = 10^{20}$ m^{-3}.
(b) Calculated profile for $\theta_{cer} \approx 65°$, $|D| = \frac{1}{2}|S|$ and $\Delta/f = 1$; fair agreement with measured profile.
(c) Static fields only: large difference in π and σ spectra.
(d) $\theta_{cer} = 0°$: 0 and 1 components dominate in σ spectrum; 2, 3 and 4 in π spectrum.

line). In Figs. 12 and 13 a comparison is made between measured and various calculated profiles for resonant ($\Delta/f \approx 1$) and non-resonant ($\Delta/f \approx 0.8$) conditions. The calculated profile can optimally be accounted for by the measured one especially in view of the intensities of the Stark components in the two polarizations, when the dynamic fieldstrength is chosen approximately half the quasi-static value and the vertex angle of the Cerenkov cone between 25 and 65 degrees.

VI. Final Conclusions

We have described a method for the calculation of hydrogen line profiles under the influence of combined static and harmonically oscillating electric fields. Experimental profiles from turbulent heating experiments can be compared with calculated ones because the fields from ion-acoustic waves may be taken as quasi-static and the fields of Langmuir waves as harmonically oscillating. We find field-strengths of $2-5\times10^6$ V/m for the ion-acoustic fields and $1-2\times10^6$ V/m for the high frequency oscillations. The energy in the oscillations varies from 1‰ to 1% of the thermal energy, depending on the plasma density and on the applied electric field. These fluctuation levels, W, are in fair agreement with data obtained from the effective collision frequency $\nu_{eff} = .3\,(W/n\,k\,T)\,\omega_{pe}$ as can be independently derived from the measurement of the anomal-

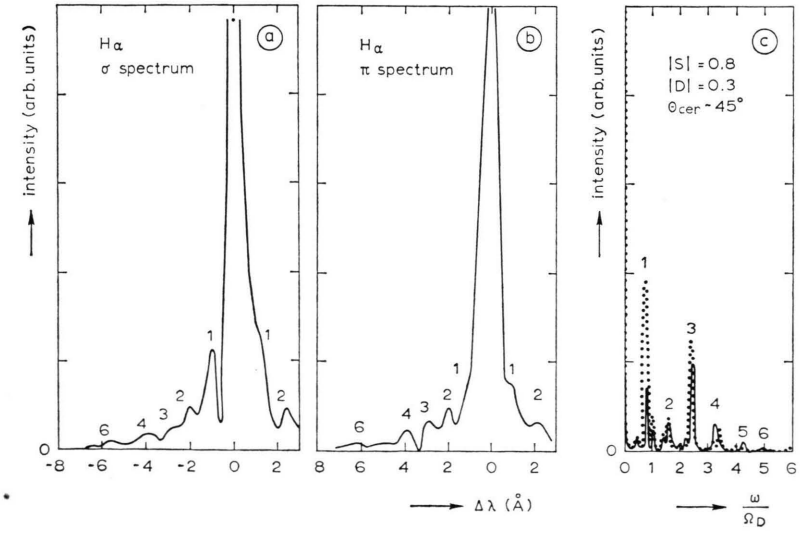

Fig. 13. Measured H_α profile for $E_0 = 28$ kV/m, $n = 10^{20}$ m^{-3}.
(a) σ spectrum,
(b) π spectrum,
(c) calculated profile for $\Delta/f = 0.8$; $\theta_{cer} \approx 45°$.
Note that the calculated component 3 is sharp. The integrated intensity is nearly the same as the intensity of component 2.

ous resistance [12]. Furthermore, the angle of the Cerenkov cone, in which the ion-acoustic waves can grow unstable, can be derived from the intensity of Stark components in different polarizations. We find a value between 25 degrees and 65 degrees yielding a ratio for the drift velocity u to the sound speed c_s of $u/c_s = 1.1 - 2.4$. This value agrees with an experimental value of $u/c_s = 1.4$ as found in Reference [11].

Acknowledgements

The authors are grateful to Dr. H. de Kluiver for his effective contribution to the development of this work and for many helpful comments and suggestions. We also wish to acknowledge the discussions with Prof. C. M. Braams and Dr. H. Schrijver and the skillful assistance in the measurements of Messrs. R.A.A. Ambags and B. de Groot.

This work was performed as part of the research programme of the association agreement of Euratom and the "Stichting voor Fundamenteel Onderzoek der Materie" (FOM) with financial support from the "Nederlandse Organisatie voor Zuiver-Wetenschappelijk Onderzoek" (ZWO) and Euratom.

[1] Zavoisky et al., Proc. of the 4th Conf. on Plasma Physics and Contr. Nucl. Fusion Res., Madison 1971, IAEA-CN-28/E-1. — S. M. Hamberger et al., IAEA-CN-28/E-3, Madison 1971. — A. B. Berezin et al., IAEA-CN-28/E-8, Madison 1971. — H. W. Piekaar et al., Proc. of the 5th European Conf. on Plasma Physics and Contr. Nucl. Fusion, Grenoble (France) 1972, Vol. 1, 147.
[2] R. Chodura, Proc. of Int. Congr. on Waves and Instab. in Plasmas, Innsbruck (Austria) 1973, Survey Lecture Ch.
[3] G. V. Sholin, Sov. Phys.-Doklady **15**, 1040 [1971].
[4] D. G. Yakovlev, Sov. Phys.-Tech. Phys. **17**, 1248 [1973].
[5] A. Cohn et al., Phys. Rev. Letters **29**, 324 [1972].
[6] C. C. Gallagher and M. A. Levine, Phys. Rev. Letters **30**, 897 [1973].
[7] W. R. Rutgers and H. De Kluiver, Z. Naturforsch. **29 a**, 42 [1974].
[8] E. Schrödinger, Ann. d. Phys. **80**, 437 [1926].
[9] H. A. Bethe and E. E. Salpeter, Quantum Mechanics of One- and Two-electron atoms, Springer-Verlag, Berlin 1957.
[10] H. A. Blochinzew, Phys. Z. Sov. Union **4**, 501 [1933].
[11] H. W. Piekaar, Rijnhuizen Report R.R. 71—67 [1971].— H. W. Piekaar, Plasma Phys. **15**, 565 [1973].
[12] H. Schrijver, Physica **70**, 339 and 358 [1973].
[13] H. Schrijver et al., Proc. of the 5th Conf. on Plasma Physics and Contr. Nucl. Fusion Res., Tokyo 1974, IAEA-CN-33/C3-1 (in press).
[14] M. V. Babykin et al., Sov. Phys. JETP **38**, 86 [1974].
[15] M. Raether and M. Yamada, Phys. Letters **44 a**, 241 [1973].